Resistance is *not* futile: The use of projections for resistance joining of metal additively and conventionally manufactured parts

Pablo D. Enrique *[a], Christopher DiGiovanni [a], Ningyue Mao [a], Robert Liang [a], Stephen Peterkin [b], Norman Y. Zhou [a]

* Corresponding Author: pdenriqu@uwaterloo.ca

[a] University of Waterloo, 200 University Ave W, Waterloo, Ontario, N2L 3G1, Canada.

[b] Huys Industries Ltd., 175 Toryork Drive, Unit 35 Weston, Ontario, M9L 1X9, Canada.

This is an author generated post-print of the article:

P.D. Enrique, C. DiGiovanni, N. Mao, R. Liang, S. Peterkin, N.Y. Zhou, Resistance is not futile: The use of projections for resistance joining of metal additively and conventionally manufactured parts, J. Manuf. Process. (2021).

The final citeable publication can be found here: https://doi.org/10.1016/j.jmapro.2021.04.035

Abstract

Metal additive manufacturing processes can produce geometrically complex and lightweight components. While conventionally manufactured components are frequently assembled to form larger parts, additive manufacturing can be used to print an entire part without needing any assembly. However, additive manufacturing processes are frequently limited in the size of the part they can produce, and it is often more economically favourable to conventionally manufacture larger or simpler geometries, such as large sheets. In this study, we demonstrate the use of a resistance joining process to facilitate the assembly of additive manufactured components. Projections are designed into additive manufactured parts to allow for joining with a conventional metal sheet. Joint performance is evaluated as a function of design choices, including the type of infill, part thickness, and proximity to adjacent joints, as well as the resistance joining process parameters. High strength joints capable of withstanding an applied torque of up to 80 Nm were obtained and functional parts were assembled to a conventionally manufactured sheet as a demonstration of the process. Incorporating projections for resistance joining into the design stage of additive manufactured parts has the potential to facilitate the use of additive manufactured components in larger assemblies and broaden the adoption of additive manufacturing in industry.

Keywords: joining, additive manufacturing, resistance welding, projection welding, assembly

Graphical Abstract

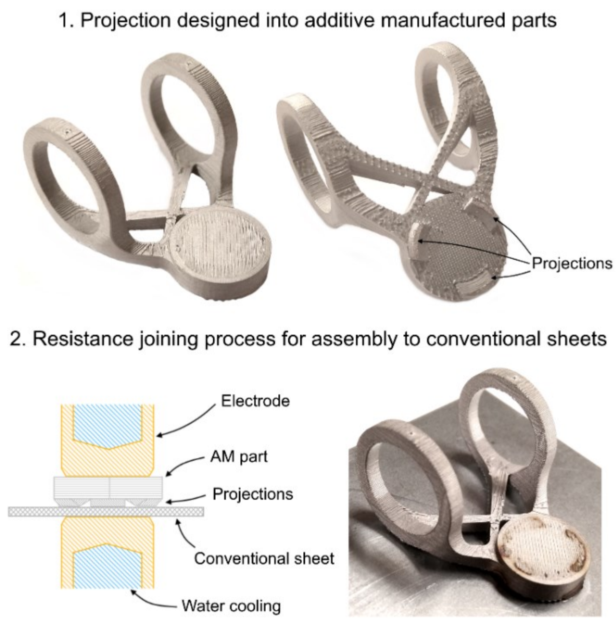

1.0 Introduction

Metal additive manufacturing processes allow for the fabrication of parts with increased geometric freedom and complex internal structures, which facilitates both lightweighting and a reduction in the number of components within an assembly. An often-discussed example is GE Aviation's advanced turboprop (ATP) engine, where an assembly of 855 conventionally manufactured parts were consolidated into just 12 parts using additive manufacturing [1,2]. This has significant benefits ranging from a dramatically simplified supply chain, a streamlined assembly of the final product, and fewer potential failure locations at welds or mechanical joints. However, there are practical limitations to printing several smaller parts as one large part. Technical considerations such as print bed size and internal stresses during manufacturing, or economic considerations such as the existence of more cost-effective manufacturing techniques for certain geometries [3], make the post-process joining of metal additive manufactured (AM) parts a critical area of study.

Mechanical joints are a common choice for applications in which the joining of AM parts is needed, although the added weight of fasteners [4] and their potential to loosen over time [5] can be detrimental to critical assemblies. Mechanical joints without fasteners have been demonstrated for AM parts by Silva et al. [6], instead using AM tenons to form mortise-and-tenon joints between metal/metal or metal/plastic combinations. With respect to welded assemblies, their generally higher strengths are preferred when higher performance joints are needed. The feasibility of joining AM parts with various geometries using welding techniques has been frequently studied in the literature.

Simple joints between plates were demonstrated by Chen et al. [7] using electron beam welding and by Singh et al. [8] using friction stir welding. Joining of more complicated AM geometries were demonstrated by Wits et al. [9] using laser welding, Huysmans et al. [10] using gas tungsten arc welding, and Nahmany et al. [11] using magnetic pulse welding, all of which join cylindrical AM parts radially or concentrically to AM or conventional counterparts. Literature studies reveal the role of AM microstructure - such as porosity and microsegregation [12] – on welding processes, often needing different parameters than those used to join conventional materials. However, these studies also make clear the need for manufacturers to consider the location of mating surfaces and their accessibility when more complicated parts need to be joined.

Some techniques are particularly suited for joining larger mating surfaces or thicker components. Traditional techniques such as laser, electron beam, or arc welding are often limited to fillet welds along the accessible edges. However, Basile et al. [13] joined an AM titanium alloy to a conventional steel shaft in a simulated turbocharger assembly, using electron beam brazing to melt a filler nickel alloy foil between the two mating surfaces. Davies et al. [14] demonstrated a similar technique using a powder interlayer and induction heating to join two mating surfaces. These two techniques use temperatures below the melting points of either of the parts to be joined and can be used to obtain larger area joints than fillet welding techniques. However, both techniques require pre-processing of the surfaces to be joined. Machining to achieve low surface roughness and tight tolerances is required for the brazing process, and diffusion bonding with a powder interlayer requires long bonding times, very clean surfaces, an inert atmosphere, and specialized fixtures to ensure adequate spacing and contact pressures. An alternative low-cost, rapid process that provides flexibility in joining thicker AM components without needing shielding gas or surface pre-processing would be preferred.

Projection welding is a technique frequently used in the automotive industry for the joining of fasteners [15,16], metal sheets [17], or components [18] to metal sheets. It functions by passing a current through distinct contact points along the mating surfaces, with localized heating, melting, and solidification joining the two parts together. Zhang et al. [19] have demonstrated the use of an additive arc process to print these contact points – also known as projections – on metal sheets, allowing them to be welded together. Rather than use a separate process to manufacture the projections, the present research proposes the design of AM parts with these projections already incorporated. An analysis of projection welding process parameters and part design is performed for the joining of solid and lattice infill AM parts to conventional materials. Joint strength and joint area are evaluated to provide guidelines for the use of projection welding as a joining technique for the assembly of AM parts.

2.0 Materials and methods

2.1 Metal additive manufacturing process and part design

Additive manufactured 17-4 stainless steel (17-4 SS) parts were made using a metal fused filament fabrication (FFF) process on a Markforged Metal X printer. The 1.85 mm diameter filament used is a proprietary blend of polypropylene (2-4%), paraffin and hydrocarbon waxes (2-6%), and 17-4 SS powder, which was printed with a nozzle temperature of 220 °C and a measured build plate temperature of approximately 50 °C. Printed parts were then washed in an Opteon SF79 solvent for at least 12 hours, until a mass loss of at least 4.1% was measured. A furnace debinding step was performed in 5.0 grade Ar gas, and sintering was performed in a 2.9% H_2 / bal. Ar atmosphere for a total heat treatment time of 25 h. A post-sintered layer height of 0.125 mm was used, along with 1 mm outer wall thickness, 0.25 mm interior wall thickness, and 0.5 mm roof and floor thickness.

The printed, washed, and sintered hexagonal test parts used for optimization of the resistance joining process and mechanical testing are shown in Figure 1a,b, with cross sections showing the triangular lattice infill in Figure 1c and solid infill in Figure 1d. A three projection design was used, with the projection dimensions based on those of a common M6 projection welding nut [15]. The FFF printed parts are automatically scaled up by the Markforged Eiger software to compensate for changes during sintering, which in this case corresponded to a shrinkage of approximately 17% measured in the xy-plane and approximately 19% measured in the z-plane. To evaluate the effect of part thickness on joint properties, hexagonal test parts with 7.4 and 11.1 mm thickness were also printed and compared to the 3.7 mm thick part shown in Figure 1b. Additionally, AM parts with lattice infill were created with two adjacent sets of projections to evaluate the effect of proximity in sequentially made joints. Joint spacings of 20, 40, and 60 mm were chosen as shown in Figure 1e and joined at three currents (6.5, 9, 11.5 kA), a force of 4 kN, and a time of 117 ms.

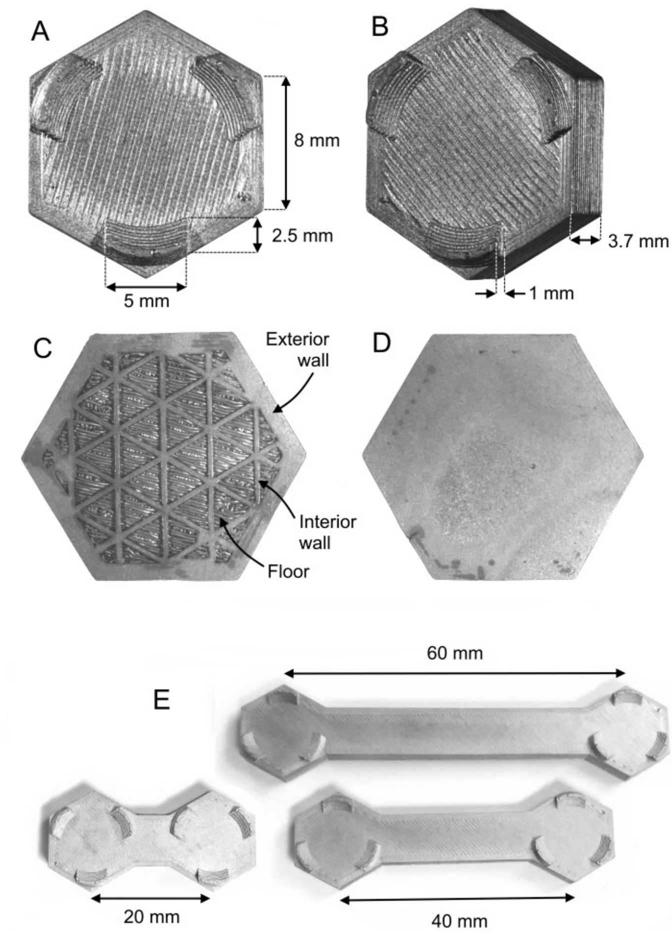

Figure 1. Hexagonal test AM parts showing a,b) general dimensions, c) a cross-section of the lattice infill, d) a cross-section of the solid infill, and e) dual joint lattice infill parts used for joint proximity testing

The proposed joining technique was demonstrated on two lattice infill components printed using the metal FFF process, including a tube guide (Figure 2a) with a single set of three projections, and a generatively designed engine mount bracket (Figure 2b) with four sets of three projections. These components are commonly joined using fasteners, but were designed or modified with projections for this study in Fusion 360 and FreeCAD.

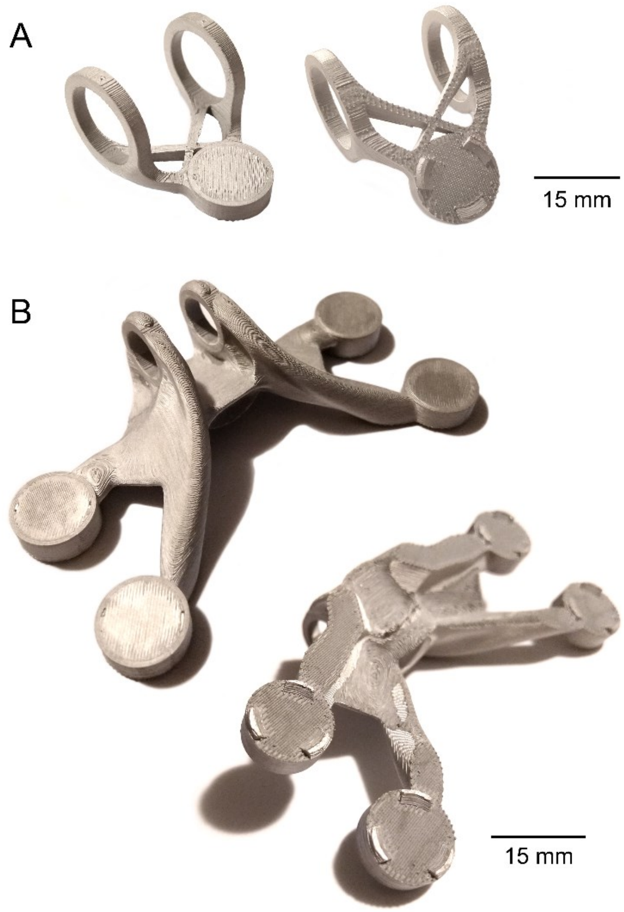

Figure 2. Functional parts demonstrating the use of projections, including a) a tube guide and b) a generatively designed engine mount bracket

2.2 Principles of resistance joining with projections and experiment design

Resistance joining processes involve the passing of a current through conductive parts, during which the bulk resistance results in heat generation along the current path and contact resistance results in heat generation at the interfaces. The inclusion of projections along the mating interface localizes heat generation by constricting the current through small contact points. As a result, projections facilitate the joining of thicker parts which would otherwise dissipate heat too rapidly to form a joint. A schematic of the projection joining process is shown in Figure 3, which uses two water-cooled class II copper electrodes with 14 mm diameter faces applied on the top and bottom of the parts being joined. This process was performed using a medium frequency direct current (DC) resistance welder, during which a current and force are applied through the electrodes for a predetermined duration. No surface preparation was performed on the samples prior to joining.

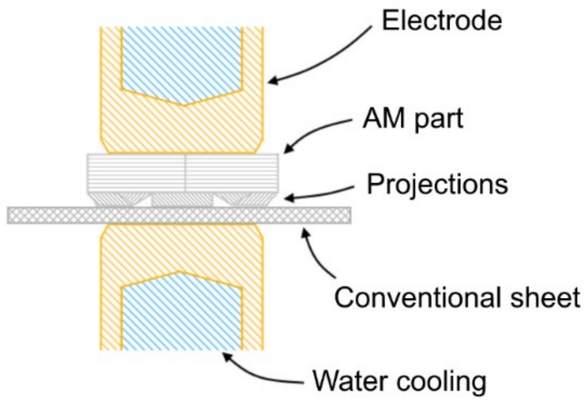

Figure 3. Schematic of joining process for the hexagonal test AM parts to a conventional sheet

Table 1 lists the parameters used to investigate the effect of current, force, and time on the properties of test coupons (Figure 1a-d) joined to a 1 mm thick conventionally manufactured galvanized steel sheet (DP 600). The experiments used a three-factor five-level circumscribed central composite design (20 rows and 6 centre points) with an α of 1.682 and one replicate. Joint strength and joint area are both measured as response variables and the analysis was performed using Develve software (version 4.11.0.0).

Table 1. Experiment design and values of current, force, and time parameters used in this study

Factors	Central Composite Design	Lattice	Solid	
		Low Energy	Low Energy	High Energy
Current (kA)	+1.682	11.5	11.5	17.5
	+1	10.5	10.5	16.5
	0	9.0	9.0	15.0
	-1	7.5	7.5	13.5
	-1.682	6.5	6.5	12.5
Force (kN)	+1.682	5.3	5.3	5.3
	+1	4.8	4.8	4.8
	0	4.0	4.0	4.0
	-1	3.3	3.3	3.3
	-1.682	2.7	2.7	2.7
Time (ms)	+1.682	173	173	284
	+1	150	150	250
	0	117	117	200
	-1	83	83	150
	-1.682	61	61	116

A response surface methodology was implemented to quantify the effect of the parameters and their interactions on joint area and joint strength. Each central composite experiment design was evaluated separately, such that separate results were obtained for solid and lattice infills at low and high energy parameters. To determine which process parameters significantly ($p < 0.05$) influenced the response variable, the parameter with the largest p value was removed, the remaining p values were pooled, and the processes was repeated until only significant parameters remained. To quantify the effect of each parameter on the response variables, a last R^2 approach was used. A last R^2 approach is performed by determining the decrease in R^2 for each parameter were it to be removed from the model, representing the individual contribution from each parameter towards explaining the variance in the experimental data.

2.3 Characterization and testing

Joint strength was evaluated using a manual torque wrench, which measures the applied torque required for joint failure. The fractured surface was imaged using a stereo microscope to measure the fracture surface area in ImageJ. Etching of joined samples was performed using Nital and a swabbing technique, for an average time of 10s. An Oxford BX51M optical microscope was used to image the resulting grain structure. Microhardness measurements were obtained with a Wolpert Wilson 402 MVD micro Vickers hardness tester using a 200 g load and 10 s dwell time.

3.0 Results and Discussion

3.1 Joint structure

The effect of heat generation on the microstructure of the DP 600 sheet is shown in Figure 4. A transformation from the sheet's original dual phase (ferrite and martensite) microstructure to one dominated by martensite in the heat-affected zone (HAZ) matches a measured increase in hardness from 217 ±10 HV to 418 ±13 HV. The dark transition region between the unaffected base metal and the HAZ corresponds to a hardness gradient shown in Figure 5, which has been previously attributed to a gradient in the fraction of martensite [20]. Welded dual phase steels frequently exhibit a sub-critical heat affected zone (SCHAZ), in which the hardness falls below that of the base metal. Only one measurement fits this description, along the boundary of the transition region and the unaffected base metal. This suggests that the SCHAZ size in the DP 600 after joining was minimal.

Although hardness within the HAZ is consistent, the microstructure near the sheet/projection interface shows significant coarsening from longer exposure to higher temperatures. The lack of directional solidification suggests that the DP 600 sheet does not melt during the joining process. This is further supported by two additional observations. Firstly, melting of the sheet alongside the projection would have resulted in a region with a mixed composition, such that the etchant would not show a clear boundary between the two materials. Secondly, the observation of 17-4 SS penetration along DP 600 grain boundaries, as indicated in Figure 4, is only possible if the DP 600 sheet remains solid throughout the joining process as the projection melts. Within the 17-4 SS AM part, the hardness remains relatively consistent (392 ±12 HV), with some potential softening within 200 µm of the 17-4 SS and DP 600 boundary. This results in a hardness slightly lower than that of the DP 600 HAZ and 1.8 times harder than the original base metal DP 600.

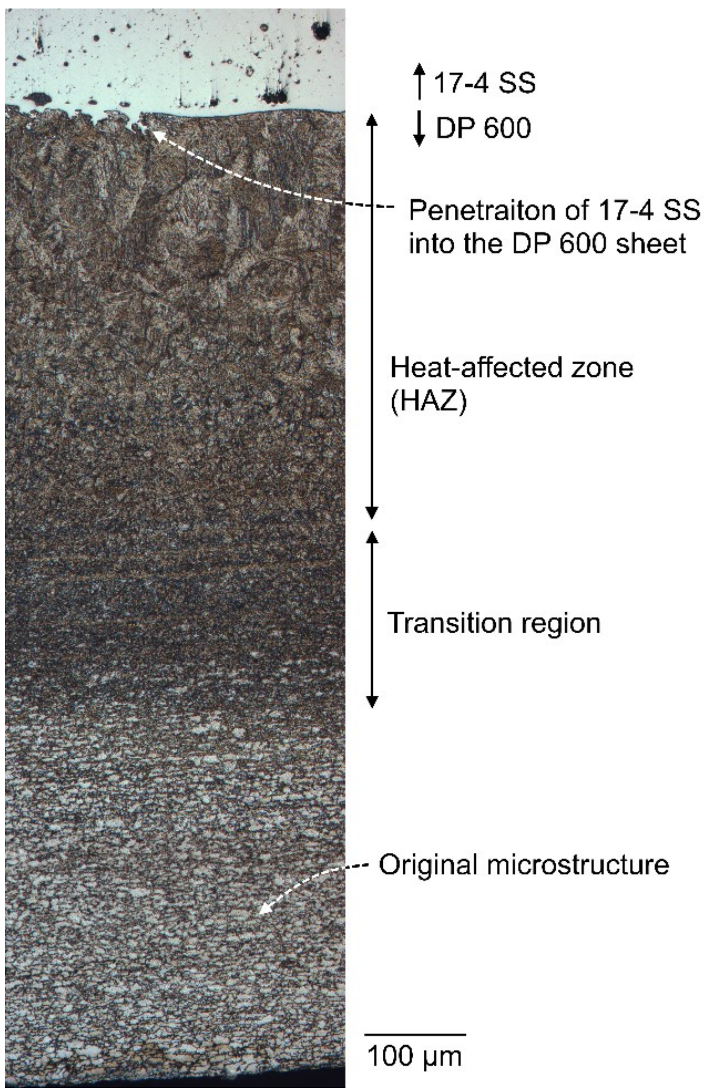

Figure 4. Etched microstructure in the conventional DP 600 sheet after joining to a hexagonal test AM part with solid infill. Process parameters used were 15 kA, 4 kN, and 200 ms.

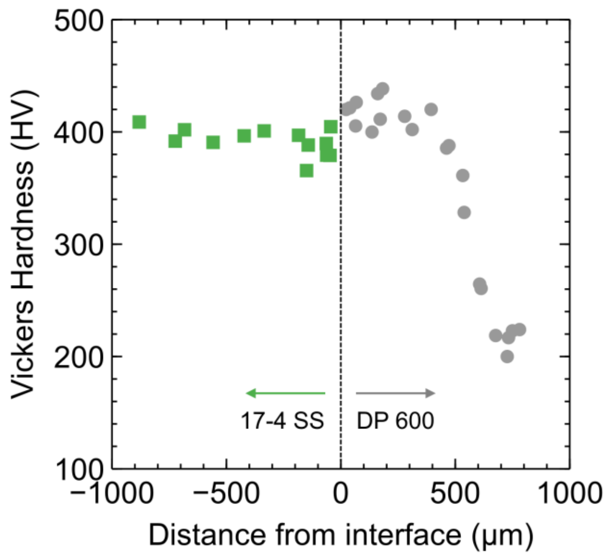

Figure 5. Hardness measurements after joining in the 17-4 AM part and the DP 600 sheet as seen in Figure 4

With process parameters that result in limited heat generation, the observed melting and deformation is restricted to the projection rather than the AM part or sheet. As shown in Figure 4, joint formation occurs due to the molten projection wetting across the sheet surface. This results in limited indentation of the projection into the sheet and no deformation of internal structures if a lattice is used (Figure 6a,c). As energy input is increased, both the amount of heat generated and the extent of projection melting increases. Although this is expected to result in higher strength joints, excessive heat generation can cause the collapse or deformation of the AM part, as shown in Figure 6b for a lattice infill. Parts printed with solid infills retain their structural integrity (Figure 6d) and can be acceptably joined with parameters that result in greater joint area and greater overall joint strength. Therefore, in addition to the process parameters that typically govern joint performance, several geometrical factors including part infill, part thickness, and proximity of adjacent joints will be discussed in the following sections.

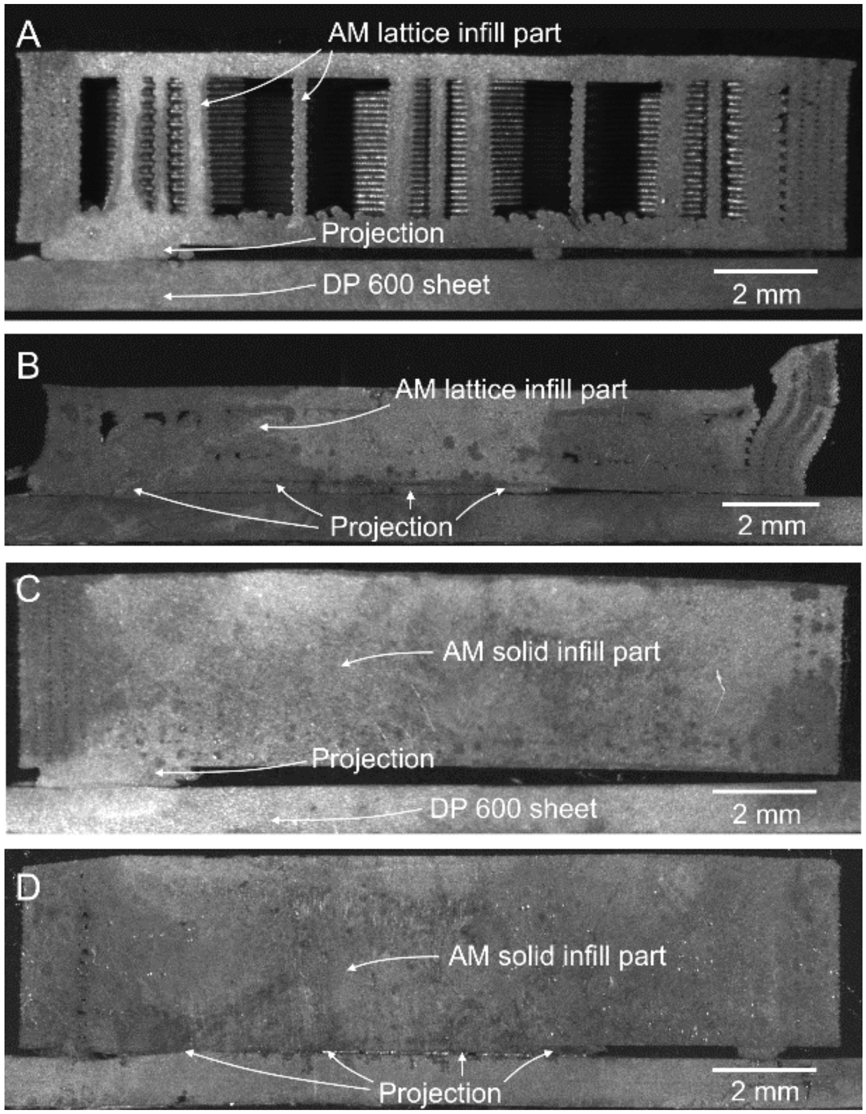

Figure 6. Optical images of AM hexagonal test coupon cross-sections with a) lattice infill joined using 9 kA, 4 kN, 116.7 ms, b) lattice infill joined using 15 kA, 4 kN, 200 ms, c) solid infill joined using 9 kA, 4 kN, 116.7 ms, and d) solid infill joined using 15 kA, 4 kN, 200 ms

3.2 Effect of process parameters

The resistance joining of an AM part with projections to a metal sheet makes use of localized contact resistance at the projection/sheet interface to melt and collapse the projection. The extent of projection collapse is dependent on the amount of heating, which is controlled by process parameters including current, force, and current duration (time). Heat generation (Q) due to joule heating and constriction resistance at each projection is governed by the following equation:

$$Q = \left(\frac{I}{n}\right)^2 \int_0^t R_T(t)dt \qquad (1)$$

The total current (I) is split across the number of projections (n) assuming they act as parallel resistors in the circuit formed during joining. The resistance (R_T) is temperature dependent, which changes with time (t) as the joint forms. Temperature is directly proportional to material resistivity, which affects the amount of joule heating, while material softening and melting leads to an increase in the contact area between the projection/sheet interface, which reduces the contact resistance. Although the force applied by the electrodes during the joining process does not directly appear in Equation 1, it also affects heat generation as part of the R_T term. An increased force should result in greater contact area at the projection/sheet interface and reduce the resistance, generating less heat.

A comparison of the influence of current, force, and time parameters on the joint performance is shown in Figure 7. Each point is an average of the full range of joints created with the process parameter of interest, and distinctions are made for low/high energy input and solid/lattice infill. At low energy input, an increase in current results in an increase in joint strength for both lattice and solid infills. This effect can be attributed to the observed increase in joint area, which results in stronger bonding between the AM part and the sheet. The trend is less clear at higher energy input, with the observed increase in joint area offset in some samples by the occurrence of molten material expulsion during resistance joining that can lead to defects. The remaining two process parameters appear to have a lesser influence on either strength or joint area.

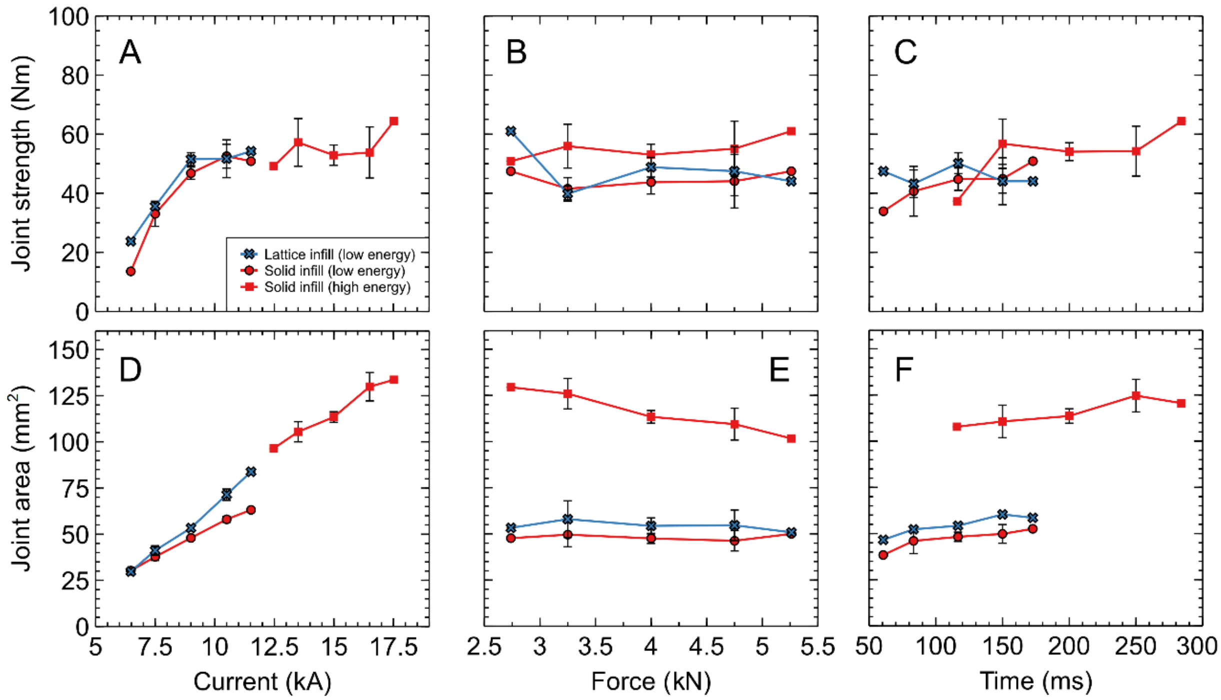

Figure 7. The effect of a) current, b) force, and c) time on joint strength and the effect of d) current, e) force, and f) time on joint area, showing standard error bars, and separated by infill type and energy input according to Table 1

The relationships obtained between process parameters (current, force and time) and joint area using up to a second-order polynomial model are shown in Table 2, with the model statistics shown in Table 3. These models fit the measured joint area data for lattice and solid infills with a high degree of accuracy, regardless of whether high or low energy input was used. This is quantified with the high R^2 values for the joint area models in Table 2 (>0.87), the predicted vs. actual joint area values in Figure 8a falling closely along the 45° line, and the standardized residuals for the predicted joint areas in Figure 8b falling mostly within two standard deviations of the actual value (and none above three standard deviations). Current is found to be a significant parameter in all response models and is the factor with the greatest influence according to the last R^2 calculation. This corresponds well with the data visible in Figure 7, which shows current has the clearest effect on both joint strength and area. In two of the models, the amount of heat generation – measured by the joint area – is positively related to the square of current as expected from Equation 1. The small coefficients for the squared current terms (0.26 and 0.7) suggest that curvature is minimal over the current range investigated in this study. This minimal curvature is also reflected in the third model, which showed only a slightly better fit using a linear current term versus a quadratic term (R^2 = 0.94 and 0.92, respectively).

The appearance of time and force as significant process variables in some of the models also followed the expected relation to heat generation, with time having a positive coefficient and force a negative coefficient.

Models created for joint strength have significantly poorer fit than those for joint area and were therefore not included. A comparison of Figure 7a and d shows that the joint area influences the joint strength only for the low energy process parameters, with no notable effect for the high energy process parameters. Unlike joint area – which is purely a function of heat generated at the interface – joint strength is a function of joint area, quantity and location of defects, and amount of material loss due to expulsion. Since the occurrence of defects and expulsion is probabilistic and is not solely determined by process parameters, the low R^2 values obtained in those models prevent drawing useful conclusions.

Table 2. Response surface model results for joint area

Response variable	Infill	Energy input	Process variable	Coefficient	*p* value	Last R^2	Model fit (R^2)
Joint Area	Solid	Low		-22.16			0.94
			Current	6.66	< 0.001	0.87	
			Time	0.086	< 0.001	0.07	
		High		100.07			0.87
			Force	-16.71	< 0.001	0.37	
			Force x Time	0.029	0.001	0.12	
			Current²	0.26	< 0.001	0.50	
	Lattice	Low		4.12			0.95
			Current x Force	-0.58	0.003	0.04	
			Force x Time	0.029	0.001	0.06	
			Current²	0.7	< 0.001	0.64	

Table 3. Statistics for models in Table 2

Response variable	Infill	Energy input	ANOVA	Degrees of freedom	Sum-of-squares	Mean squares	F ratio	*p* value
Joint Area	Solid	Low	Regression	2	1476.35	738.17	125.53	< 0.001
			Error	17	99.97	5.88		
			Total	19	1576.31			
		High	Regression	3	3277.25	1092.42	35.33	< 0.001
			Error	16	494.66	30.92		
			Total	19	3771.91			
	Lattice	Low	Regression	3	3559.27	1186.42	98.02	< 0.001
			Error	16	193.67	12.1		
			Total	19	3752.94			

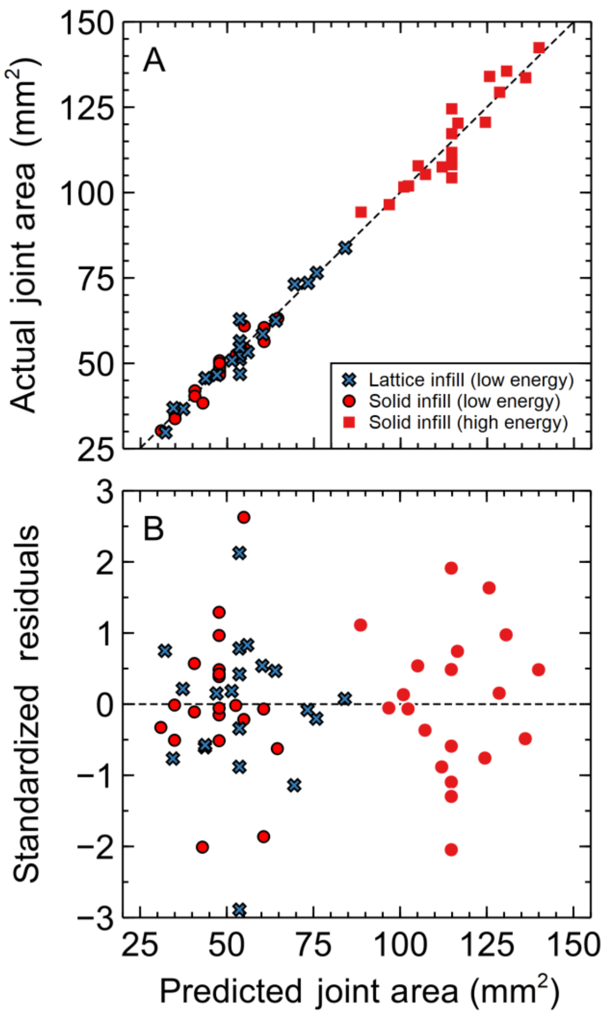

Figure 8. A comparison of actual and predicted results using the response surface model for a) joint area and b) the associated standardized residuals for the joint area predictions

3.2 Effect of infill type

A comparison of infill patterns in Figure 7 shows lattice infills often generate higher strength joints and larger joint areas than solid infill using low energy parameters. Dynamic resistance curves obtained during joining reveal the physical processes responsible for the difference in joint properties. Each dynamic resistance curve is a sum of two main underlying curves, one of which describes the contact resistance at the projection/sheet interface and the other which describes the bulk resistance in the AM part and the sheet. Assuming no surface film is present, the contact resistance first increases as the current reaches the set point and the temperature at the projection/sheet interface rises, and then decreases as the projection softens and melts. At the same time, the bulk resistance increases as temperature increases within the sheet and AM part [21]. During the initial joint formation period

(Figure 9a), parts with a lattice infill demonstrate a higher resistance than solid infill parts. Higher temperatures and reduced heat conduction away from the projection/sheet interface is expected in lattice infill parts due to the smaller solid volume and significant void space located adjacent to the interface. This has the effect of increasing temperatures, increasing electrical resistivity, and increasing the observed resistance, corresponding to the lattice infill AM parts having greater joint areas and greater strength.

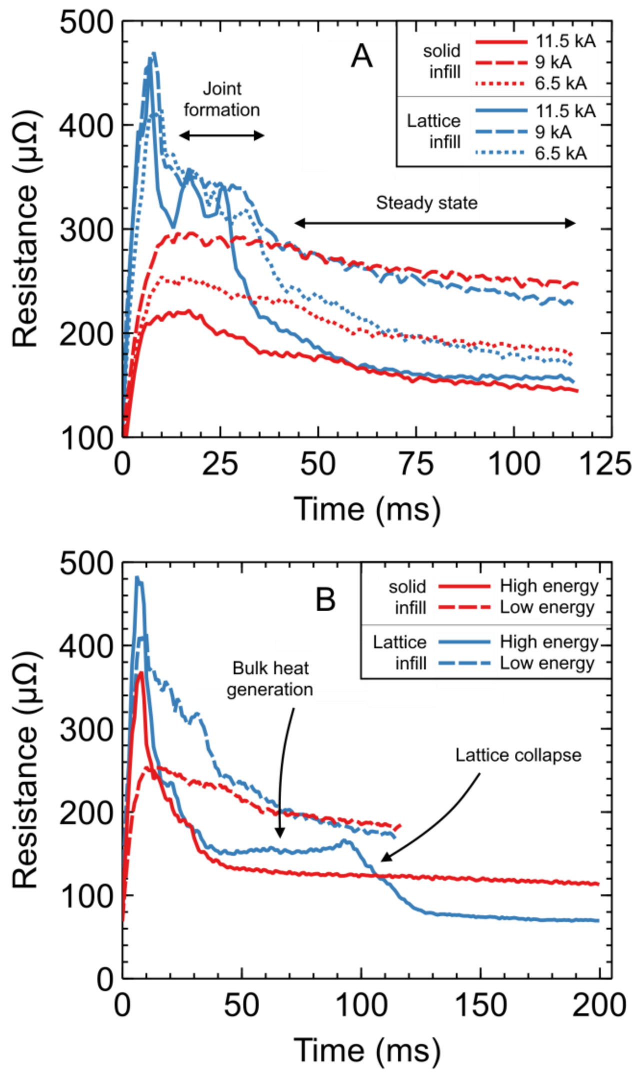

Figure 9. Dynamic resistance curves for solid and lattice infill samples created with a) 4 kN, 117 ms, various currents and b) low energy (9 kA, 4 kN, 117 ms) and high energy (15 kA, 4 kN, 200 ms) parameters

Although there are notable initial differences in the resistance curves, the long-term resistance converges for both lattice and solid infill samples joined with the same current at low energy input. In this steady-state region, heat generation occurs primarily in the bulk of the sheet and AM part, with the contact resistance at the projection/sheet interface having been significantly reduced when the joint was formed. The small change in resistance over time suggests that the steady-state temperature distribution is being approached. However, this is not true for the high energy lattice infill part shown in Figure 9b. Heat generation outpaces heat conduction in the lattice, causing an increase in temperature and electrical resistivity that is measured as an increase in dynamic resistance. The resistance continues to increase until a sufficiently high temperature is reached and the internal lattice structure collapses under the force of the electrodes (Figure 6b), corresponding to the drop in resistance observed in Figure 9b.

3.2 Effect of part thickness

The amount of material between the two copper electrodes, defined by the sheet thickness, projection height, and AM part thickness, can be expected to vary depending on AM part design and application constraints. Therefore, the effect of increasing part thickness on the joint must be understood to develop appropriate design guidelines. The dynamic resistance curves in Figure 10 show the effect of increasing AM part thickness from 3.7 mm to 11.1 mm. The resistance of a conductor is directly proportional to the current's path length, such that an increased thickness has the expected result of increasing the resistance. In the steady state region of the resistance curve for solid infill parts joined with low energy input (Figure 10a), each 3.7 mm increase in part thickness corresponded to an increase of approximately 22 μΩ. As such, the contribution to the overall resistance from the part thickness can be taken as 22, 44, and 66 μΩ in the 3.7, 7.4, and 11.1 mm thick AM parts, respectively. The rest of the measured resistance is primarily attributed to bulk resistance of the sheet, contact resistance from the remaining interfaces (electrode/AM part and electrode/sheet), and bulk resistance in the collapsed projections.

In the initial non steady-state region of the dynamic resistance curves in Figure 10b,c, it is possible to observe the effect of thickness on the projection/sheet interface. These AM parts with 3.7 mm thickness show initial spikes in the dynamic resistance curve. This corresponds well with joint area as seen in Table 4, especially in the case of the solid infill parts joined using high energy parameters (Figure 10c) which had a more pronounced spike in resistance. The greater melting in these thinner AM parts is attributed to their smaller mass, which can more quickly achieve higher temperature required to form a larger joint.

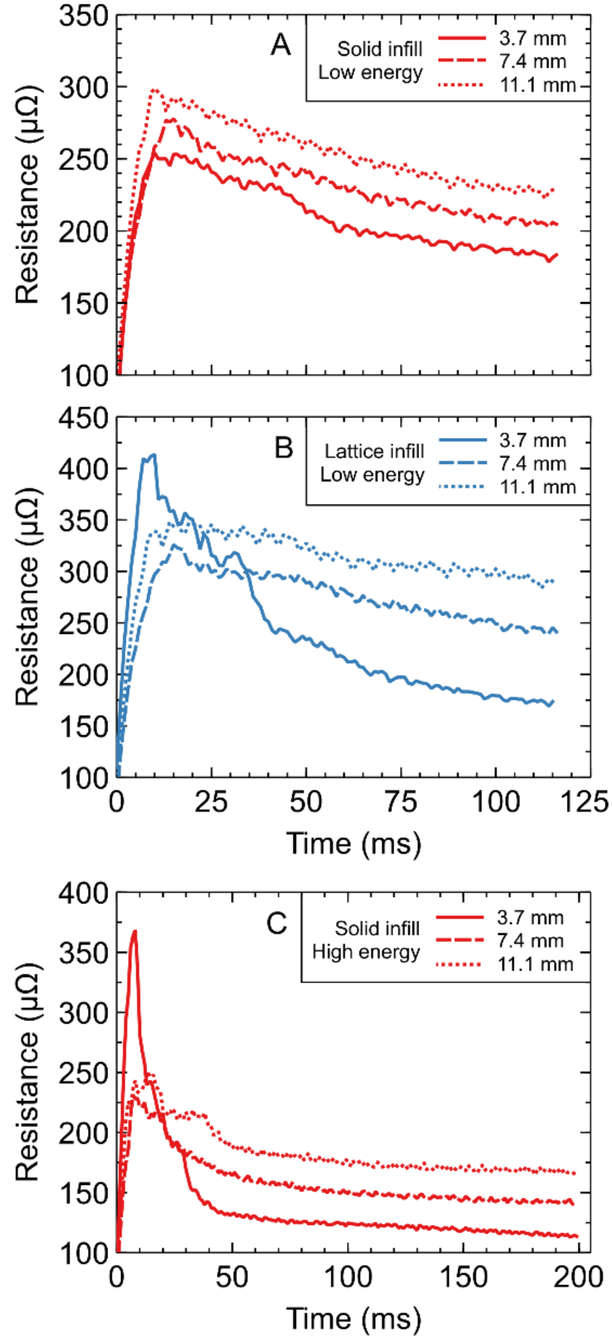

Figure 10. Effect of thickness on dynamic resistance curves for a) solid infill and low energy (9 kA, 4 kN, 117 ms), b) lattice infill and low energy (9 kA, 4 kN, 117 ms), and c) solid infill and high energy (15 kA, 4 kN, 200 ms)

Table 4. Joint areas for AM parts with different thickness

	Low Energy		High Energy
Thickness (mm)	Solid infill (mm^2)	Lattice infill (mm^2)	Solid infill (mm^2)
3.7	48.5	54.1	112.6
7.4	46.1	50.7	78.9
11.1	45.8	52.0	88.5

3.3 Effect of adjacent joints

The use of adjacent sets of projections may be necessary for joining larger parts or where additional load bearing capacity on a part is required. Sequential joining of projection sets are simpler to perform, since simultaneous joining of all projection sets requires the development of more complex electrodes and equipment capable of delivering higher currents. However, during sequential joining (Figure 11a), projection collapse in the first set can cause deformation of the underlying sheet (Figure 11b) due to constraints imposed by the unmelted neighboring projections. If the joints are too close together or the sheet is too stiff, the sheet may not be able to bend sufficiently to accommodate the unmelted projections, and incomplete projection collapse may occur in the first joint. When a subsequent joint is formed, stress can be introduced into the initial joint (Figure 11c) as the sheet attempts to conform to the second joint. Additionally, the second joint may experience shunting, in which a portion of the current passes through the first joint. In spot welding processes, thicker sheets and higher contact resistance increases the minimum spacing needed to avoid shunting [22]. Dynamic resistance curves of three AM parts that were not successfully joined are shown in Figure 12a-c, while three representative results from the six successfully joined AM parts are shown in Figure 12d-f. Since each AM part tested here contains two sets of three projections (Figure 1e), each graph contains two dynamic resistance curves – one for the first set of projections, and another for the second set.

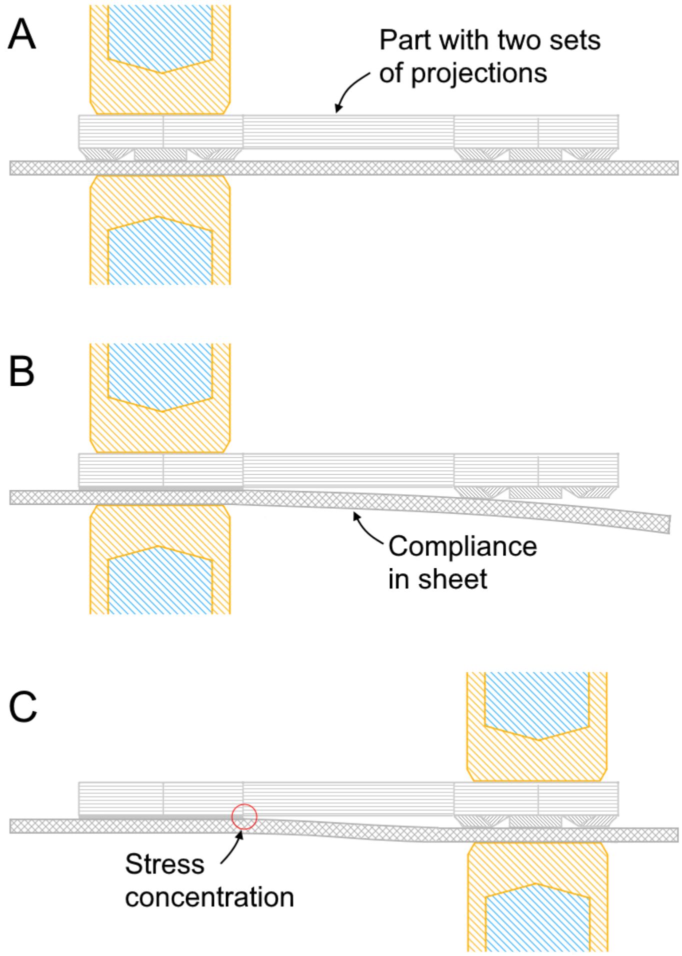

Figure 11. Influence of adjacent projections on geometric constraints during a) clamping of first set of projections, b) welding of first set of projections, and c) clamping of second set of projections

In the case of a 20 mm spacing between sets of projections joined at the lowest current of 6.5 kA (Figure 12a), the first set of projections fell apart immediately after welding without any applied force. For the AM part with 60 mm spacing joined at 6.5 kA (Figure 12b), the first joint broke while the electrodes applied their clamping force to the second set of projections. In both cases, failure of the first joint is attributed to geometric constraints by the neighbouring set of projections and suggests that the strength of the first joint is insufficient. At higher currents, one sample joined at 9 kA with 20 mm spacing failed (Figure 12c). In this case, the first joint failed with no applied force as the sample was cooling. In all cases where joint failure was observed, the first joint was always the one that failed. Low current, small spacing, and a combination of the two were the factors contributing to joint failure. As both were increased, joints strong enough to withstand geometrically induced stresses were formed.

When compared to properly joined AM parts with two sets of projections (Figure 12d-f), the failed parts all show deviations towards higher resistance at the end of the weld in the first joint when compared to the second joint. This is not observed in parts where both joints remain bonded, with the dynamic resistance curves converging more closely. This is attributed to less melting and collapse at the interface in the first joint, which results in a higher resistance. Additionally, the dynamic resistance curves do not show evidence of current shunting for any of the tested spacings, which would appear as a consistently lower resistance in the second joint [23].

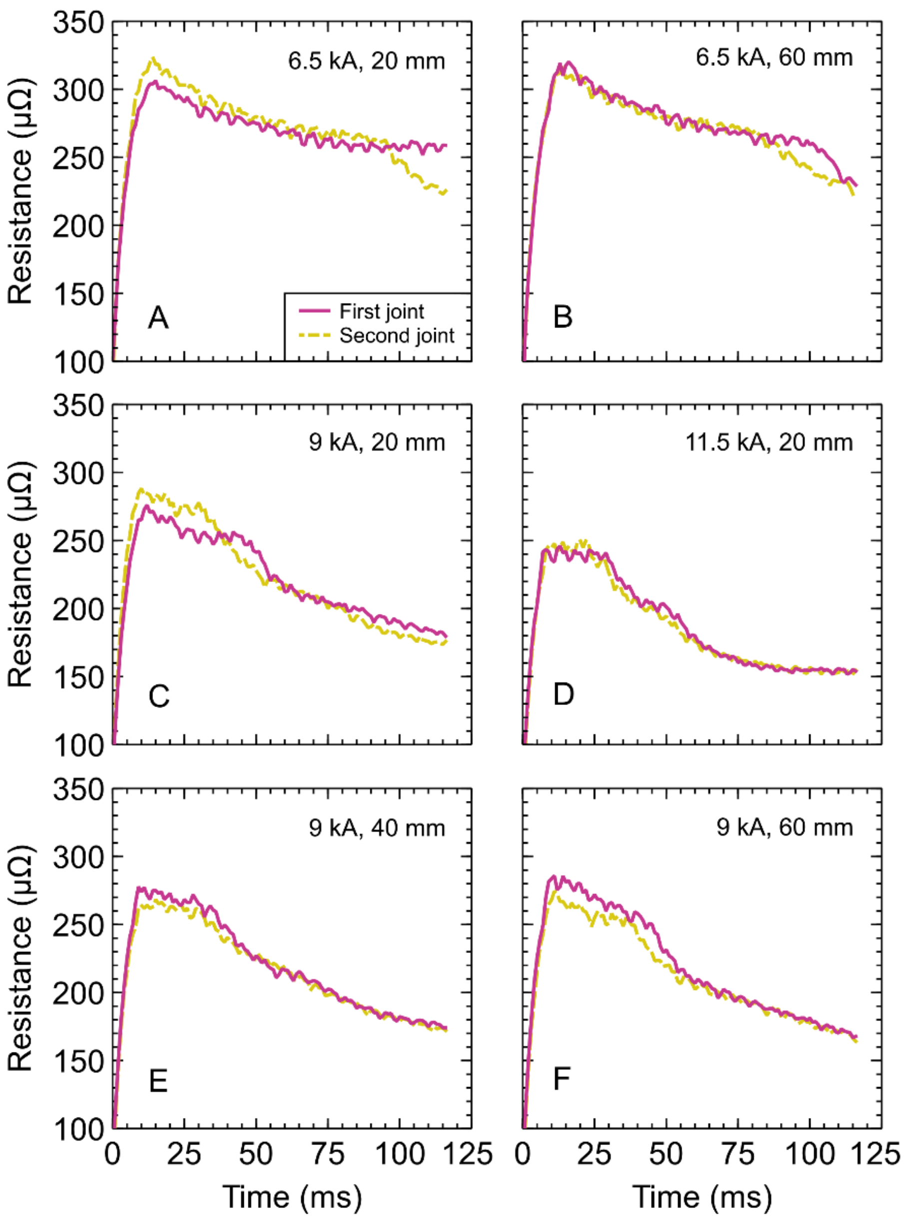

Figure 12. Dynamic resistance curves for AM parts with two joints as shown in Figure 1e. Each graph indicates the current used for joining and the joint spacing.

3.4 Extension of results to functional parts

Findings from the hexagonal test AM parts are extended to functional AM parts (Figure 2) with two projection configurations. These parts – which contain lattice infills – were joined to a DP 600 sheet using 11.5 kA, 4 kN and 117 ms. For parts with lattice infill, this relatively high current ensures a significant amount of melting at the projection/sheet interface and a high strength joint, although the parts can be seen to experience heating and oxidation at the electrode/part interface (Figure 13). The use of lower parameters when lower joint strength is required results in less or no visual discoloration of the top surface.

The tube guide in Figure 13a was designed to allow for easy electrode access to the joining area by excluding the area above and around the joint from the design space. Additionally, it only uses a single joint with three projections to avoid any issues from adjacent sets of projections. The result is an easily joined part with no significant challenges, and a dynamic resistance curve with the same characteristics as the hexagonal test pieces demonstrated previously. However, the joining of an engine mount bracket which uses four sets of three projections (shown in Figure 13b) proved to be significantly more challenging.

The sequential joining of four sets of three projections resulted in significant residual stresses that compromised one of the four joints. This can be observed using the dynamic resistance curves shown in Figure 13b. The first two joints, both having a thickness of 5.5 mm, were created successfully and show a very similar dynamic resistance curves. The third and four joints, which have a thickness of 6.3 mm and a correspondingly higher steady state resistance, can be seen to deviate from each other towards the end of the weld. Although all joints were initially successful, joint 3 failed when a manual force was applied. This suggests that stresses introduced during the sequential joining of adjacent sets of projections can be significantly detrimental to the weld integrity, and that the parameters identified as acceptable for the joining of two adjacent joints in Section 3.3 cannot be freely extended to designs with more than two joints. To overcome this limitation, it is recommended that designs aim to incorporate only one joint. If multiple joints are needed, two solutions are proposed: ample spacing must be incorporated into the design between all joints to minimize stress buildup, or all joints must be welded simultaneously to prevent stress buildup.

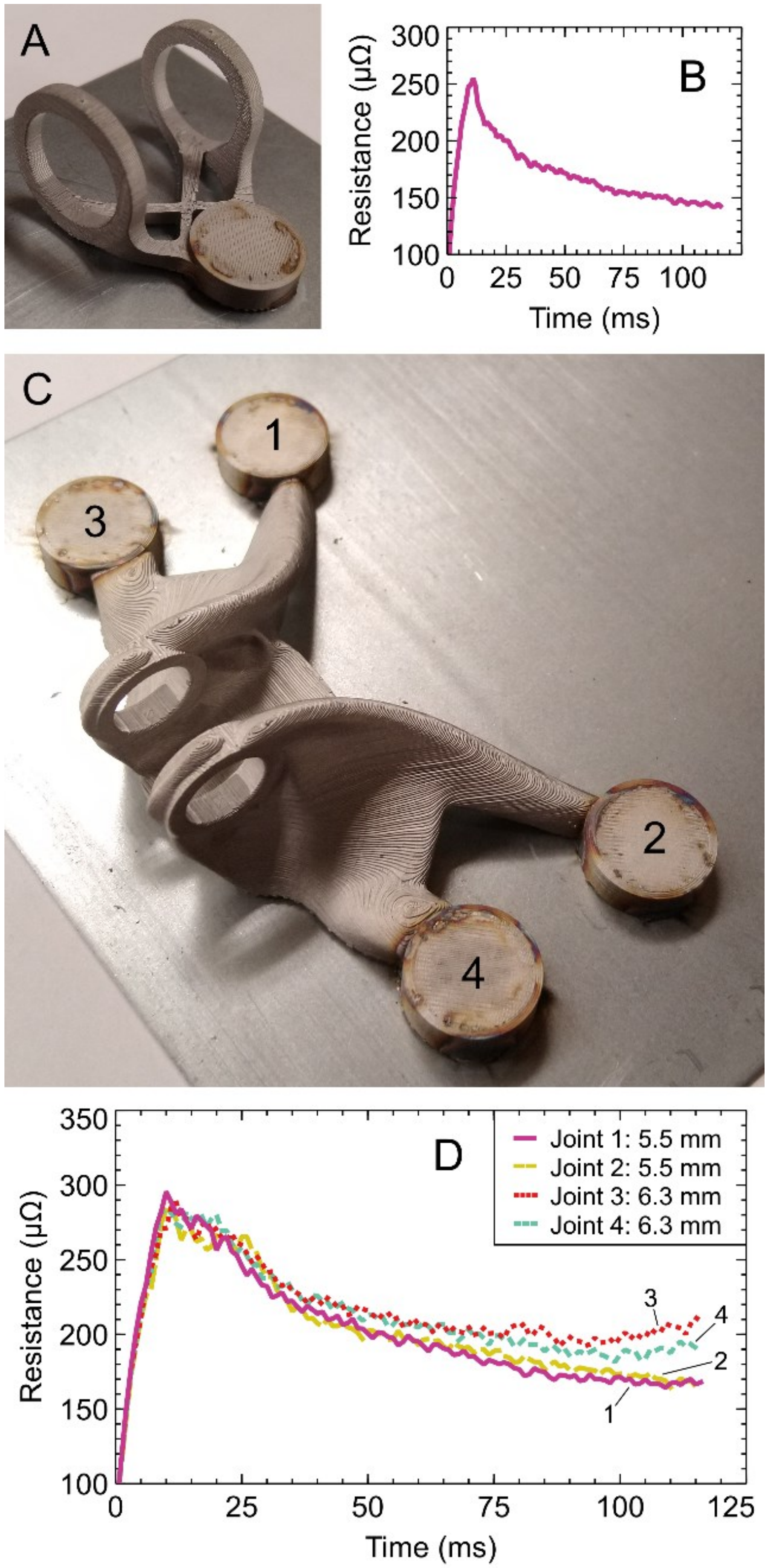

Figure 13. Example joints for a) a tube guide, with b) dynamic resistance curve, and c) a generatively designed engine mount bracket with two joint thicknesses, with d) dynamic resistance curves

4.0 Conclusions

The addition of projections to additive manufactured (AM) components was demonstrated as a viable approach to enable the assembly of AM parts using resistance joining. Several AM part design considerations and the resistance joining process parameters were investigated for their influence on joint performance. The following considerations are suggested when implementing this assembly technique:

1. The main resistance joining process parameters – current, force, and time – showed the expected relation to heat generation, which was positively related to the square of the current, negatively related to the force, and positively related to the time. Current had the largest effect within the range of parameters studied, and response surface models created to relate process parameters with the joint area all showed good fit ($R^2 > 0.87$).
2. The amount of material in the AM part influences the amount of melting at the projection. AM parts designed with lattice infills can obtain greater joint areas and joint strengths with the same process parameters. However, the internal lattice was also found to collapse when high energy input was used, while parts with solid infills retain their structural integrity.
3. Thicker AM parts were found to increase the bulk resistance during joining, however thinner parts resulted in greater melting at the interface and larger joint areas.
4. If more than one joint is needed, the proximity of adjacent joints can affect joint area and strength. With small spacing between adjacent joints, geometrical constraints can result in incomplete projection collapse or the introduction of stresses when the second joint is welded. An increase in current and an increase in spacing were both shown to overcome the geometrical constraints from two adjacent joints. However, limitations were demonstrated when extending these findings to a greater number of adjacent joints.

Acknowledgements

This work was performed with funding support from the Natural Sciences and Engineering Research Council of Canada (NSERC), Huys Industries, and the CWB Welding Foundation, at the Centre for Advanced Materials Joining at the University of Waterloo.

References

[1] Kellner T. Fired Up: GE Successfully Tested Its Advanced Turboprop Engine With 3D-Printed Parts. GE News 2018. https://www.ge.com/news/reports/ge-fired-its-3d-printed-advanced-turboprop-engine (accessed November 8, 2020).

[2] Brown AS. Chain Reaction. Mech Eng 2018;140:30–5. https://doi.org/10.1115/1.2018-OCT1.

[3] Massoni B, Campbell MI. Optimizing Cutting Planes for Advanced Joining and Additive Manufacturing. J Manuf Sci Eng Trans ASME 2018;140:1–9. https://doi.org/10.1115/1.4038509.

[4] Goh GD, Agarwala S, Goh GL, Dikshit V, Sing SL, Yeong WY. Additive manufacturing in unmanned aerial vehicles (UAVs): Challenges and potential. Aerosp Sci Technol 2017;63:140–51. https://doi.org/10.1016/j.ast.2016.12.019.

[5] Jiang Y, Zhang M, Park T-W, Lee C-H. An Experimental Study of Self-Loosening of Bolted Joints. J Mech Des 2004;126:925–31. https://doi.org/10.1115/1.1767814.

[6] Silva DFM, Bragança IMF, Silva CMA, Alves LM, Martins PAF. Joining by forming of additive manufactured ‘mortise-and-tenon’ joints. Proc Inst Mech Eng Part B J Eng Manuf 2019;233:166–73. https://doi.org/10.1177/0954405417720954.

[7] Chen X, Zhang J, Chen X, Cheng X, Huang Z. Electron beam welding of laser additive manufacturing Ti–6.5Al–3.5Mo–1.5Zr–0.3Si titanium alloy thick plate. Vacuum 2018;151:116–21. https://doi.org/10.1016/j.vacuum.2018.02.011.

[8] Singh AK, Kumar B, Jha K, Astarita A, Squillace A, Franchitti S, et al. Friction stir welding of additively manufactured Ti-6Al-4V: Microstructure and mechanical properties. J Mater Process Technol 2020;277:116433. https://doi.org/10.1016/j.jmatprotec.2019.116433.

[9] Wits WW, Jauregui Becker JM. Laser beam welding of titanium additive manufactured parts. Procedia CIRP 2015;28:70–5. https://doi.org/10.1016/j.procir.2015.04.013.

[10] Huysmans S, Peeters E, De Bruycker E, De Prins K. Weldability study of additive manufactured 316L austenitic stainless steel components—welding of AM with conventional 316L components. Weld World 2021. https://doi.org/10.1007/s40194-021-01098-z.

[11] Nahmany M, Shribman V, Levi S, Ashkenazi D, Stern A. On Additive Manufactured AlSi10Mg to Wrought AA6060-T6: Characterisation of Optimal- and High-Energy Magnetic Pulse Welding Conditions. Metals (Basel) 2020;10:1235. https://doi.org/10.3390/met10091235.

[12] Emmelmann C, Beckmann D-IF. Optimization of laser welding process for laser additive manufactured aluminum parts by means of beam oscillation and process-oriented component design. Lasers Manuf., 2017.

[13] Basile G, Baudana G, Marchese G, Lorusso M, Lombardi M, Ugues D, et al. Characterization of an additive manufactured TiAl alloy-steel joint produced by electron beam welding. Materials (Basel) 2018;11:3–11. https://doi.org/10.3390/ma11010149.

[14] Davies P, Johal A, Davies H, Marchisio S. Powder interlayer bonding of titanium alloys: Ti-6Al-2Sn-4Zr-6Mo and Ti-6Al-4V. Int J Adv Manuf Technol 2019;103:441–52. https://doi.org/10.1007/s00170-019-03445-3.

[15] Enrique PD, Al Momani H, DiGiovanni C, Jiao Z, Chan KR, Zhou NY, et al. Evaluation of Electrode Degradation and Projection Weld Strength in the Joining of Steel Nuts to Galvanized Advanced High Strength Steel. J Manuf Sci Eng 2019;141:1. https://doi.org/10.1115/1.4044253.

[16] Nielsen C V., Zhang W, Martins PAF, Bay N. 3D numerical simulation of projection welding of square nuts to sheets. J Mater Process Technol 2015;215:171–80. https://doi.org/10.1016/j.jmatprotec.2014.08.017.

[17] Papkala H. An investigation into the processes of projection welding of galvanised sheet. Weld Int 1996;10:5–13. https://doi.org/10.1080/09507119609548941.

[18] Zhu WF, Lin ZQ, Lai XM, Luo AH. Numerical analysis of projection welding on auto-body sheet metal using a coupled finite element method. Int J Adv Manuf Technol 2006;28:45–52. https://doi.org/10.1007/s00170-004-2336-8.

[19] Zhang G, Zhao H, Xu X, Qiu G, Li Y, Lin Z. Metallic bump assisted resistance spot welding (MBaRSW) of AA6061-T6 and bare DP590: Part I-printing of metallic bump. J Manuf Process 2019;44:427–34. https://doi.org/10.1016/j.jmapro.2019.05.042.

[20] Pouranvari M, Marashi SPH, Mousavizadeh SM. Dissimilar resistance spot welding of DP600 dual phase and AISI 1008 low carbon steels: Correlation between weld microstructure and mechanical properties. Ironmak Steelmak 2011;38:471–80. https://doi.org/10.1179/1743281211Y.0000000024.

[21] Wang SC, Wei PS. Modeling dynamic electrical resistance during resistance spot welding. J Heat Transfer 2001;123:576–85. https://doi.org/10.1115/1.1370502.

[22] Li YB, Wang B, Shen Q, Lou M, Zhang H. Shunting effect in resistance spot welding steels - Part 2: Theoretical analysis. Weld J 2013;92.

[23] Xing B, Xiao Y, Qin QH. Characteristics of shunting effect in resistance spot welding in mild steel based on electrode displacement. Meas J Int Meas Confed 2018;115:233–42. https://doi.org/10.1016/j.measurement.2017.10.049.